Noninvasive white blood cell quantification in umbilical cord blood collection bags with quantitative oblique back-illumination microscopy

Paloma Casteleiro Costa [1], *Patrick Ledwig,* [2] *Austin Bergquist,* [2] *Joanne Kurtzberg,* [3,4] *and Francisco E. Robles* [1,2]

BACKGROUND: Umbilical cord blood has become an important source of hematopoietic stem and progenitor cells for therapeutic applications. However, cord blood banking (CBB) grapples with issues related to economic viability, partially due to high discard rates of cord blood units (CBUs) that lack sufficient total nucleated cells for storage or therapeutic use. Currently, there are no methods available to assess the likelihood of CBUs meeting storage criteria noninvasively at the collection site, which would improve CBB efficiency and economic viability.

MATERIALS AND METHODS: To overcome this limitation, we apply a novel label-free optical imaging method, called quantitative oblique back-illumination microscopy (qOBM), which yields tomographic phase and absorption contrast to image blood inside collection bags. An automated segmentation algorithm was developed to count white blood cells and red blood cells (RBCs) and assess hematocrit. Fifteen CBUs were measured.

RESULTS: qOBM clearly differentiates between RBCs and nucleated cells. The cell-counting analysis shows an average error of 13% compared to hematology analysis, with a near-perfect, one-to-one relationship (slope = 0.94) and strong correlation coefficient (r = 0.86). Preliminary results to assess hematocrit also show excellent agreement with expected values. Acquisition times to image a statistically significant number of cells per CBU were approximately 1 minute.

CONCLUSION: qOBM exhibits robust performance for quantifying blood inside collection bags. Because the approach is automated and fast, it can potentially quantify CBUs within minutes of collection, without breaching the CBUs' sterile environment. qOBM can reduce costs in CBB by avoiding processing expenses of CBUs that ultimately do not meet storage criteria.

Over the past 3 decades, umbilical cord blood (UCB) has been used as an alternative source of hematopoietic stem and progenitor cells (HSPCs) for transplantation for patients lacking a fully matched donor.[1,2] HSPCs can also be extracted from bone marrow and mobilized peripheral blood, but collection from these sources of HSPCs exposes donors to lengthy procedures that carry risks of infection, bleeding, and localized pain.[3] Collection of UCB, on the other hand, poses no risks to the mother or newborn child. In addition, the use of UCB for therapy/transplants has a reduced likelihood of transmitting infections, particularly cytomegalovirus, and after being thoroughly tested and human leukocyte antigen (HLA) typed, transplants can be stored in the frozen state,

available for immediate use.[4] Finally, partially HLA-mismatched UCB from unrelated donors can be used for transplantation with lower rates of graft-versus-host disease than the other HSPC sources.[3,5–7] These advantages have led to an increased effort to research and bank UCB to make treatments faster, more accessible, and more effective.[2,8] With close to 5 million cord blood units (CBUs) stored in public and private banks worldwide, cord blood banking (CBB) plays an increasingly important role in stem cell transplantation and other cellular therapeutics.[1,3]

Despite the aforementioned advantages, the cost of procuring CBUs is over 10 times more than peripheral blood and bone marrow, which makes it less accessible to the end user and is causing a decrease in the use of UCB for transplantation. The high cost of CBUs is due, in part, to high discard rates of CBUs before cryopreservation.[2,9] Indeed, 66% to 75% of collected CBUs fail to meet storage criteria[10,11] due to insufficient volumes,[12] delayed arrival at the processing site, and, more importantly, low total nucleated cell counts,[13,14] which correlate with poor success rates of transplant engraftment.[15]

Thus, there is an unmet need to monitor the contents of CBUs at the collection site (i.e., maternity unit) and assess the units' suitability for storage before undergoing further expensive processing at the CBB.[16] However, several unique requirements must be met to satisfy this unmet need. First, the procedure must be fast, easy to implement, and robust to be conducted at the collection site. Second, the device must be low cost and have a small footprint. Finally, the procedure must be performed in such a way that the cord blood remains under a sterile environment at all times to avoid the risk of contamination. In other words, any monitoring procedure of UCB must not breach the sterile conditions of the CBUs.

The final requirement is particularly onerous given that existing procedures to monitor blood with flow cytometry[17,18] or a hematology analyzer,[19] for example, require extraction of a blood sample from the CBU, which breaches sterility. These procedures also require extensive sample preparation or instrument calibration. Recently, sophisticated nonlinear imaging techniques have been proposed to monitor blood contents noninvasively inside storage bags,[20] but such methods require large and expensive systems and highly trained individuals to operate them.

In this work, we present a proof of principle study with a novel label-free optical imaging technique called quantitative oblique back illumination microscopy (qOBM) to monitor the contents of CBUs noninvasively. This novel imaging approach is fast, easy to use, robust, low cost, compact, and noninvasive, thus fulfilling all the unique requirements to monitor CBUs at the collection site.

qOBM provides quantitative phase information, but, unlike conventional phase imaging techniques, it can be used in thick scattering environments, including CBUs.[21,22] Traditional phase imaging technologies yield detailed (quantitative) subcellular information without labels or dyes by detecting light transmitted through a thin sample.[23] qOBM extends these capabilities by using an elegant epi-illumination scheme[24] and fast reconstruction strategy,[25] packaged into a simple inverted microscope configuration, to achieve the same level of contrast as traditional phase imaging but in thick structures tomographically.[21,22] Data from qOBM can also be processed to provide absorption-based contrast.[22,24]

Recently, we have demonstrated the ability of a dual-wavelength OBM system to image inside clear blood bags and differentiate between red blood cells (RBCs) and white blood cells (WBCs).[22] Here, we extend this framework with added quantitative capabilities[21] to monitor the contents of CBUs noninvasively (specifically, WBC and RBC counts and assess hematocrit). Note that WBC counts and total nucleated cell counts are often used interchangeably in the literature[26,27] under the assumption that they have a similar predictive value for engraftment, given that, on average, there are only 3.5 nucleated RBCs (nRBCs) per 100 WBCs in UBC, and nRBCs are not used for therapy.[28] The automated imaging approach taken here simulates a procedure that can be applied at the CBU collection site. Results from 15 CBUs show excellent agreement with the complete blood count (CBC) measurements determined by a commercial automated hematology analyzer. This approach has the potential to significantly reduce costs in CBB by avoiding expenses related to processing CBUs that ultimately do not provide therapeutic benefits or meet storage criteria for cord blood banks.

MATERIALS AND METHODS

qOBM system and image processing

The qOBM system consists of a conventional inverted microscope geometry with epi-mode illumination emanating from four diametrically opposed light sources, delivered through 1-mm plastic optical fibers (Fig. 1). The light sources sequentially illuminate the sample. When light from one of the sources is deployed into the thick scattering medium (i.e., the blood bag), light scatters multiple times, effectively producing a virtual light source within the sample and with an oblique angle. Thus, the system is effectively a transmission microscope in disguise (with four oblique light sources). In our particular configuration, the fibers are tilted by 45 degrees to increase the degree of obliquity, which enhances the sensitivity of the system.[29] Next, light is collected by an inverted microscope, equipped with a 60× microscope objective (S Plan ELWD, NA 0.7, Nikon), and detected using an sCMOS camera (4.2LT, pco.edge).

To generate quantitative phase with qOBM, we first produce differential phase contrast (DPC) images, which are similar to those produced with differential interference contrast (DIC) microscopy. This is achieved by subtracting and normalizing images acquired from two diametrically opposed sources, as described by Equation 1[25,30]
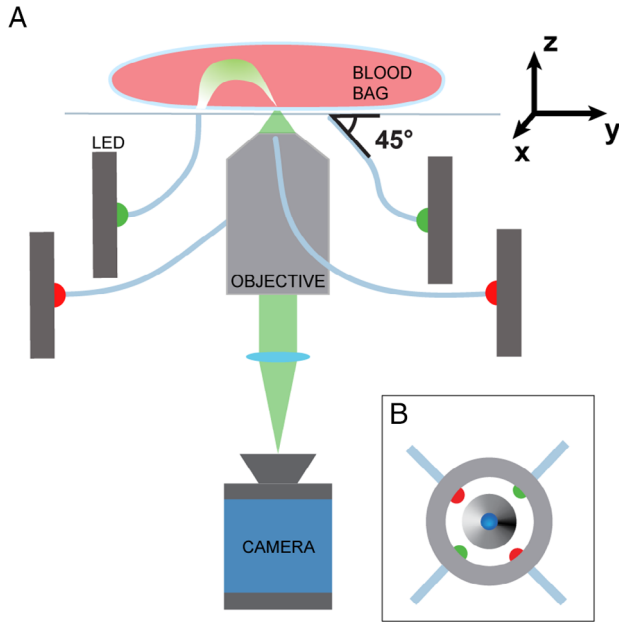
Fig. 1. Schematic of the qOBM system. (A) The blood bag sample is illuminated with four LED light sources (two red and two green) deployed through fiber optics, which are tilted by 45 degrees. The light is then collected by the objective and is then imaged by the camera. (B) Top view of the objective surrounded by the fiber holder with the four illumination fibers. [Color figure can be viewed at wileyonlinelibrary.com]

$$I_{DPC} = \frac{I_R - I_L}{I_R + I_L} \tag{1}$$

where I_R and I_L are the two images obtained with one pair of opposing sources, denoted right and left, respectively. Note that because we have four sources, we produce two DPC images, each with orthogonal shear angles to ensure high-contrast information in every direction.[25] Further, the subtraction process in Equation 1 removes the out-of-focus component, thus allowing tomographic sectioning.[24] An example DPC image is shown in Fig. 2C.

To recover quantitative phase information from the DPC images, we use a fast deconvolution algorithm that accounts for the angular distribution of light at the focal plane of the microscope.[21] Note that optical phase is a function of the wavelength (λ), the refractive index change between the sample and the medium (Δn), and the thickness of the sample (Δz), and are related as described by Equation 2:

$$\Delta \phi = \frac{2\pi}{\lambda} \Delta z \cdot \Delta n \tag{2}$$

An example qOBM image is shown in Fig. 2D, which is not only quantitative but also shows drastically enhanced contrast of cellular and subcellular structures compared to the DPC image.

In addition to the quantitative phase, we obtain absorption information at two distinct wavelengths. As shown in Fig. 1, each diametrically opposed pair of light sources has a different color: one pair is red (627 nm) and the other green (530 nm) to get access to molecular information from hemoglobin absorption, which strongly absorbs green light.[31] This identifies RBCs and nRBCs. The same captured images used to recover quantitative phase are used to obtain absorption information (i.e., transmission images). To do so, we simply add the two opposing captures corresponding to the same color:

$$I_{tx}^{green} = I_R^{green} + I_L^{green} \tag{3}$$

Therefore, in addition to the structural information obtained from the phase, we also use absorption information for segmentation and classification of different cell types (see the Automated segmentation procedure section for details).

Sample preparation and study design

For this proof-of-principle study, 15 cord blood collection bags were obtained from the Carolinas Cord Blood Bank at the Duke University Medical Center and imaged in the Optical Imaging and Spectroscopy laboratory at the Georgia Institute of Technology. Only research CBUs that did not meet storage criteria due to low collection volumes were used. Samples were imaged within 48 hours of collection.

Once samples arrived at the Optical Imaging and Spectroscopy laboratory, 250 μL of blood was transferred from the collection bags to a custom-made, clear bag (Instant Systems). The samples were diluted in the clear bag in 1% phosphate-buffered saline with a 1:100 (blood to phosphate-buffered saline) ratio, and then imaged by the qOBM system. Note that while the procedure used here does not maintain a sterile environment, future work will use an integrated bag design that includes the collection bag and the additional clear bag for imaging (with the diluent included), connected through sterile tubing. CBUs are already preloaded with anticoagulant citrate phosphate dextrose solution, and the same solution can be preloaded into the clear bag to serve as the diluent. A small amount of blood can be transferred to the clear bag in a controlled fashion while ensuring that no contaminants enter the integrated CBU. Aside from this difference in transferring the blood to the clear bag, the procedure described in this work could be used while maintaining sterility.

A CBC for each sample was obtained using an automated hematology analyzer (XN-1000 R, Sysmex), which includes flow cytometry with a semiconductor laser to perform the WBC differential. These results were used as ground truth to validate and compare our imaging and segmentation results.

Automated segmentation procedure

To enhance the accessibility of our system, we developed a fully automated image acquisition and cell segmentation
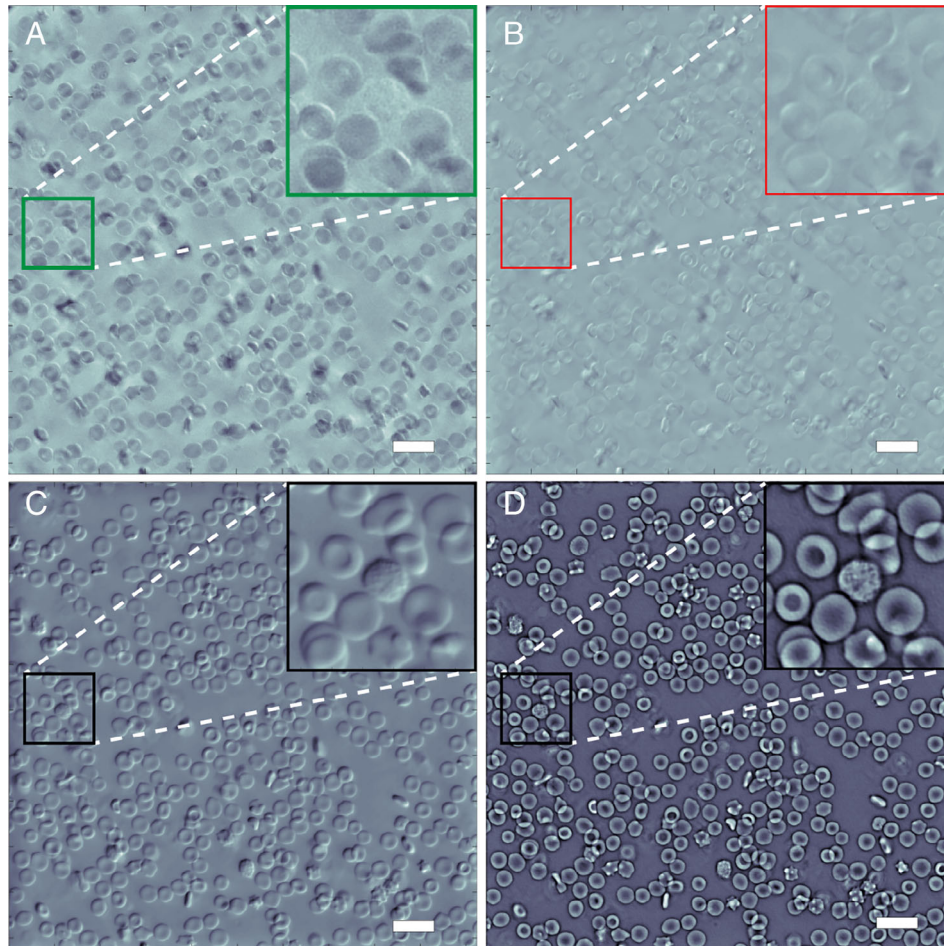
Fig. 2. Representative images of UCB inside clear collection bag obtained with a single qOBM capture sequence. (A, B) Transmission images obtained with green (530 nm) and red (627 nm) light, respectively. Inset shows RBCs and a WBC in the center. (C) Differential phase contrast at 630 nm. The DPC images obtained with green and red light have no noticeable difference other than the angle of illumination. (D) Quantitative phase image. All scale bars are 25 μm and the magnification is 60X. [Color figure can be viewed at wileyonlinelibrary.com]

procedure for counting WBCs and RBCs (see Fig. 3A). To this end, we acquire 100 images of each sample at an imaging plane corresponding to where the cells settle at the bottom of the bag. A 10×10 grid of images is obtained automatically by translating the sample in the x-y plane using an automated motorized stage. Considering the field of view of each image ($230 \times 230 \mu m$), we cover a total area of approximately 2×2 mm on the sample in approximately 1 minute.

Although the motorized stage allows precise and stable control over the position of the sample, small variations on the desired imaging plane along the z-axis (due to wrinkles on the bag or tilt) can cause the captures to be out of focus. These out-of-focus images are discarded automatically before additional processing by adding a quality assessment step. Here, we define a metric for in-focus images based on the sharpness of individual DPC images. These types of images are chosen because they contain only information along the shear direction (given by the position of the illuminating fibers). Thus, the Fourier space of in-focus DPC images shows a unique bilobed structure that is less pronounced or altogether absent for out-of-focus DPC images (see Fig. 4). Hence, for the image quality assessment, we extract the standard deviation of the angular average of the Fourier transform from 0 to π radians. Higher standard deviations indicate a more defined bilobed shape and, consequently, a better image focus. This calculation is performed as the first step of the segmentation process to reject any images that do not meet our image quality criteria. Autofocusing could be included in future work.

The images that pass the quality check are then processed with a four-step algorithm that first detects individual cells and then differentiates RBCs from WBCs. False positives and false negatives in the description of the
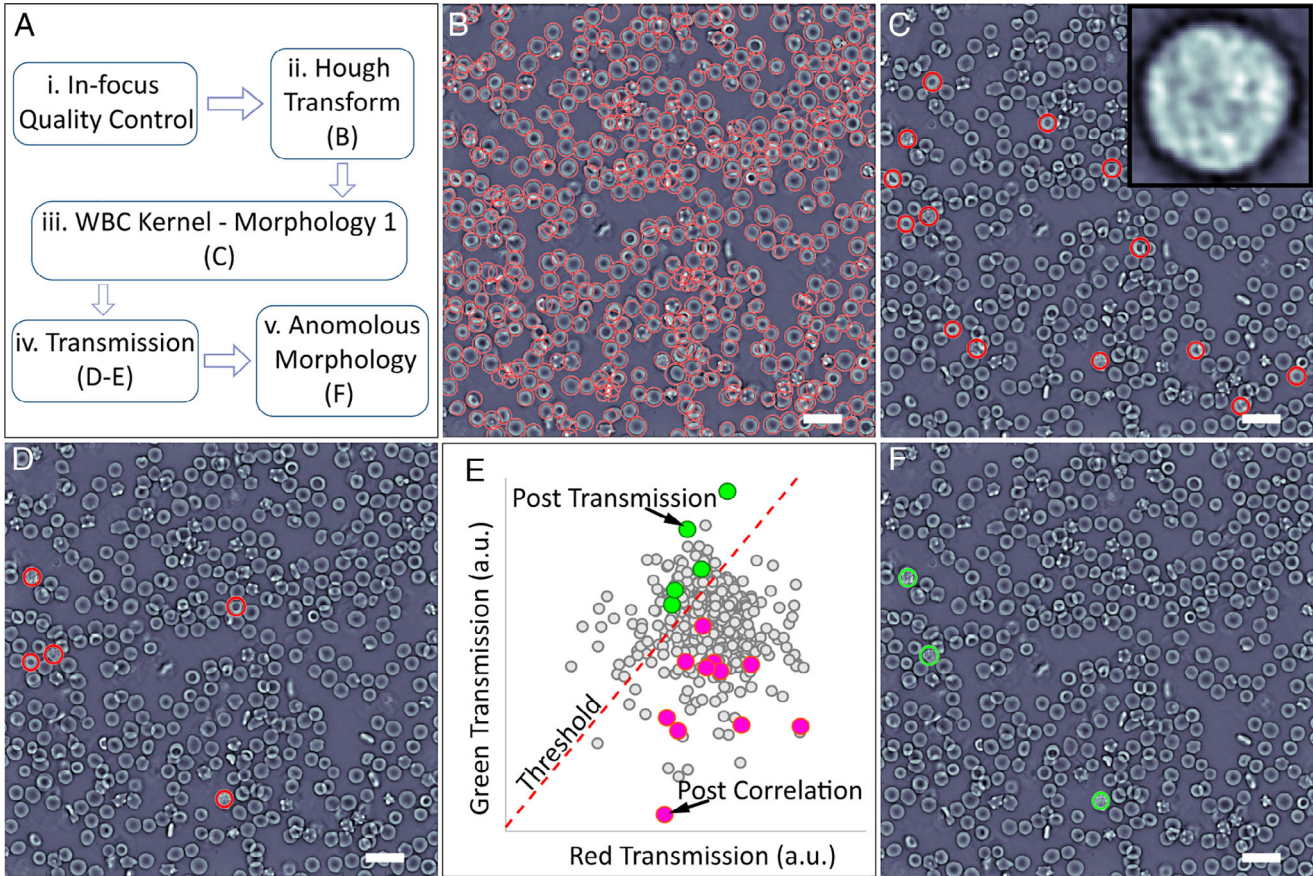
Fig. 3. Automated RBC and WBC segmentation: (A) Flow chart of processing steps. Results form (B) Hough transform, (C) kernel cross-correlation and phase WBC kernel, (D) relative transmission principal component analysis and (E) scatter plot of transmission values, and (F) morphology step. All scale bars are 25 μm and the magnification is 60x. [Color figure can be viewed at wileyonlinelibrary.com]

algorithm below, and in the results section, refer to cells that are incorrectly classified at any particular step of the automated algorithm compared to visual inspection. Final results of the algorithm (i.e., average WBC count as determined by qOBM and this automated algorithm) are quantitatively compared to results from a hematology analyzer.

In the first step of the algorithm, cell detection is done by identifying circular shapes using a Hough transform[32] from the quantitative phase images. This assumes, of course, that blood cells have a circular profile (more on this below).

Next, each cell is compared to a WBC kernel extracted from a test image. Cells with the highest morphology similarities to this kernel are selected as WBC candidates. This step is designed to have high sensitivity, allowing for a relatively high degree of false positives (RBCs passing as WBCs assessed via visual inspection) to avoid false negatives (WBCs passing as RBCs).

Once the first set of WBC candidates is selected, we evaluate the absorption of each cell under red and green light. Hemoglobin in RBCs (and nRBCs) strongly absorbs green light (530 nm) and has low absorption of red light

(627 nm), while WBCs do not strongly absorb either color. To analyze the relative absorption of each cell, we generate a scatter plot of green versus red transmission: cells with a higher green-to-red transmission are counted as WBCs. Note that WBCs stand out as outliers in the scatter plot of any image, which mainly consists of RBCs. This step uses a principal component analysis (PCA)[33] to generate a threshold that identifies outliers based on the distribution mentioned above (see Fig. 3E).[22] Here, WBC candidates must be one standard deviation away from the mean distribution along both principal components.

While the absorption analysis removes most false positives (such as nRBCs or acanthocytes), some unusually shaped cells may still be miscounted as WBCs. This includes RBCs that are not lying flat or that have a higher biconcavity, which allow more green light to be transmitted near the center of the cell. To reject these false positives, a final morphology step is applied, which takes a closer look at the morphology of each preselected cell. Those that have a biconcave shape, low circularity, or significantly high absorption patches combined with high phase value are not counted as WBCs.
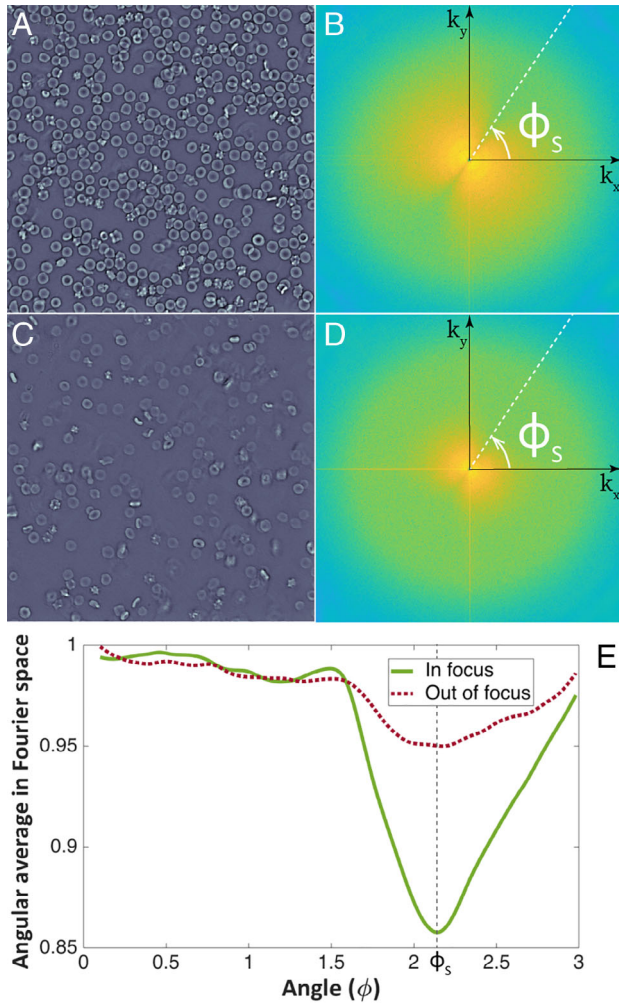
Fig. 4. In-focus image assessment. (A) Example in-focus phase image. (B) Fourier transform of corresponding DPC image in A. (C) Example out-of-focus phase image and (D) the Fourier transform of corresponding DPC image. (E) Angular average of Fourier distribution of in-focus and out-of-focus images. [Color figure can be viewed at wileyonlinelibrary.com]

Finally, we only consider samples that yield a total of 15,000 segmented cells or more. This ensures that even under the most limiting case of, say, 1 WBC per 600 RBCs (or a ratio of 1.6E-3 WBC/total cells), the error in our WBC estimate is 20% or less. Here, we assume a Poisson distribution where percent error is given by $1/\sqrt{N}$, where N is the number of WBCs (15,000 [total cells] x 1.6E-3 [WBC/total cells] = 25 [WBCs]). With each individual image containing roughly 500 cells per field of view (and again 100 images are acquired per sample), this condition is not highly restrictive for the most part.

The entire segmentation and computational analysis is packaged into a simple graphic user interface (in MATLAB, MathWorks), making the process simple and user accessible. Our developed computer program can segment and differentiate cells in the 100 acquired images in less than 3 minutes, reducing the whole process (i.e., imaging and segmentation analysis) to less than 5 minutes without requiring an Internet connection.

RESULTS

Figure 2 illustrates a representative image of UCB inside the clear bags, from each of the four different types of contrast generated from the acquired data: transmission (green and red), DPC, and quantitative phase. Each image has a size of 2048 × 2048 pixels, with an effective pixel size of 0.138 μm on the sample, corresponding to a field of view of 282 × 282 μm^2. The resolution of the system is 0.6 μm.

The images visibly show regular biconcave RBCs, acanthocytes, RBCs on their sides, and WBCs. Note that while the DPC image shows the general morphology of each cell with some subcellular detail, the quantitative phase image has much greater clarity and has enhanced conspicuity of subcellular structures of, for example, acanthocytes and the internal contents of WBCs. The transmission images noticeably differentiate between the WBCs and RBCs. Here, the absorption of red light is low and consistent across the entire image, while the green transmission confirms the expected absorption of RBCs at a wavelength of 530 nm, making the differentiation between cells containing hemoglobin and those that do not very clear.

Figure 4 shows the outcomes of each segmentation step. The results of the Hough transform, in Fig. 4A, identify all in focus cells present in the field of view. The sensitivity of the Hough algorithm was set high (0.94) to assure that cells with a close-to-circular shape, such as acanthocytes, were still selected. The autocorrelation step (Fig. 4B) performs as anticipated: it selects all WBCs and some RBCs as potential nucleated cells. Then, the absorption analysis (Fig. 4C) identifies all the WBCs with fewer—but not zero—false positives. Again, these false positives are expected, since they will be rejected by the fourth and last step of the algorithm, which accounts for internal cell morphology. For the specific example shown in Fig. 4, there are two false positives easily identifiable due to their traditional biconcave shape. Figure 4D shows the final selection of nucleated cells in the example, which now contains only WBCs without false positives.

Figure 5 plots the measured relative concentration (WBC counts relative to the total cell count) measured with our image-based approach versus those obtained in the CBC. We note that 4 of the 15 samples did not meet the total segmented cell count criteria (defined in the Automated segmentation procedure section under Materials and Methods), resulting from out-of-focus images, which can be mitigated with autofocusing in the future. The error bars in Fig. 5 are given by the square root of the number of WBCs counted, which again assumes a Poisson counting process.
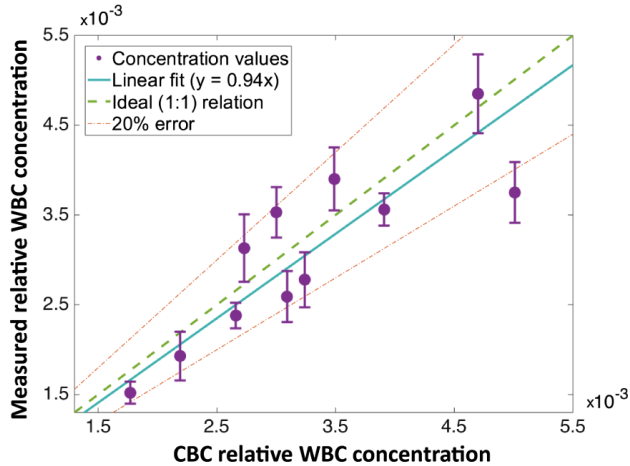
Fig. 5. Results of the pilot study. Scatter plot of measured WBC/RBC concentrations versus complete blood count concentrations. The solid blue line represents the linear fit of the results. An ideal fit would have a slope of 1 (dashed green line); the measured results have a slope of 0.94. The error bars represent the confidence intervals, based on the number of WBCs detected. The red dashed lines represent an error of 20% from the 1:1 fit. [Color figure can be viewed at wileyonlinelibrary.com]

Table 1 summarizes the results, but here the calculated error refers to the percent error between the image-based counts compared to the CBC. These results clearly show that the WBC concentrations measured with qOBM are in

agreement with the hematology analysis, maintaining an average error of 13.4%, with a standard deactivation of 5.5%. The slope of the fitted line in Fig. 5, which indicates the agreement between the noninvasive image-based approach and the CBC, is nearly perfect, with m = 0.94 (the ideal slope is 1) and a high correlation coefficient of 0.86.

The presented results show the potential of the qOBM system to acquire high-resolution images of cord blood inside clear collection bags and analyze the contents with high precision noninvasively.

DISCUSSION AND FUTURE WORK

In this work, we have shown that qOBM can accurately quantify the relative concentration of WBCs. This novel approach is noninvasive, fast, easy to use, robust, and does not require labels or stains. Components are also low cost (with the microscope objective being the most expensive component), and the device can be extremely compact. All these factors make qOBM a powerful tool to quantify CBUs at the collection site, which can potentially reduce costs associated with processing units that do not meet storage criteria, thereby making CBB more efficient and economically viable.

Future work will focus on measuring the absolute WBC count instead of providing a relative measure of the concentration. The only parameter needed to obtain this information is the effective number of imaged cells per unit volume of blood. To shed light on this issue, consider that the total WBC count (TWBCC) in the collection bag is given by Equation 4:

TABLE 1. Pilot study results					
BAG ID	Modality	Total number of cells	WBCs	Relative concentration	Concentration error (%)
120	CBC	2.84E+12	9.94E+09	3.49E-03	11.80
	qOBM	34997	137	3.90E-03	
594	CBC	2.26E+12	6.80E+09	3.00E-03	17.60
	qOBM	41806	148	3.53E-03	
677	CBC	3.24E+12	8.88E+09	2.73E-03	14.62
	qOBM	22273	70	3.13E-03	
685	CBC	2.81E+12	9.12E+09	3.24E-03	−14.05
	qOBM	29408	82	2.78E-03	
687	CBC	3.18E+12	9.86E+09	3.09E-03	−16.33
	qOBM	29694	77	2.59E-03	
728	CBC	2.85E+12	6.25E+09	2.19E-03	−11.68
	qOBM	26856	52	1.93E-03	
851	CBC	2.18E+12	1.03E+10	4.70E-03	3.18
	qOBM	25431	124	4.85E-03	
164	CBC	3.42E+12	9.13E+09	2.66E-03	−10.57
	qOBM	127783	305	2.38E-03	
611	CBC	2.94E+12	1.48E+10	5.01E-03	−25.15
	qOBM	34279	129	3.75E-03	
563	CBC	2.64E+12	1.04E+10	3.91E-03	−8.96
	qOBM	124204	444	3.56E-03	
517	CBC	3.50E+12	6.19E+09	1.77E-03	−13.67
	qOBM	104816	160	1.52E-03	

CBC = complete blood count; qOBM = quantitative oblique back-illumination microscopy.
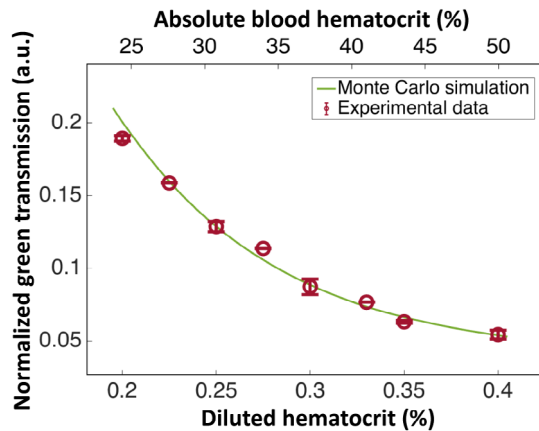
Fig. 6. Relative green transmission intensity as a function of hematocrit. The error bars are the standard deviation of the normalized transmission taken from 24 images with the same hematocrit. The solid green line represents the transmission values (detected number of photons vs. input number of photons) obtained through a Monte Carlo simulation of the system. [Color figure can be viewed at wileyonlinelibrary.com]

$$TWBCC = \frac{WBCd}{RBCd} * hct(\%) * \frac{V_b}{MCV} \qquad (4)$$

where *WBCd* and *RBCd* refer to the number of WBCs and RBCs detected in the imaged region using qOBM, *hct* is the hematocrit of the blood, V_b is the volume of blood in the CBU (measured at the collection site), and *MCV* is the mean corpuscular volume. In Equation 4, the effective cell count per unit volume is given by $hct(\%)/(RBCd \times MCV)$. Thus, in this formulation, there are two unknown parameters, hematocrit and MCV, both of which can be ascertained with qOBM.

Here, we can again leverage the fact that the green light is strongly absorbed by RBCs, leading to a predictable exponential attenuation of the overall background green light with increasing hematocrit. Further, because our green light-emitting diodes (LEDs) are centered at 530 nm, which corresponds to an isosbestic point for oxyhemoglobin and deoxyhemoglobin,[34] the measurement in the green channel is largely insensitive to oxygenation state. Figure 6 shows the average intensity values of raw image captures of a blood bag using the green LEDs, normalized by images taken with the red LEDs, before cells settled at the bottom layer. This was repeated at various dilutions to simulate the range of expected hematocrit values in cord blood (25%–40%). Because red light is much more weakly absorbed by RBCs, it serves as an internal reference where the ratio between green and red background mostly depends on hematocrit.[35] Indeed, Fig. 6 reveals a predictable exponential attenuation behavior that it is well modeled by a light transport simulation using Monte Carlo (solid line in Fig. 6).

While this calibration was not performed in the proof-of-concept experiments, Fig. 6 illustrates the ability to produce a lookup table where the ratio of the green and red images without settled cells directly yields the hematocrit of a given blood bag.

For the MCV estimates, either an average value of approximately 115 fL can be used since expected fluctuations in normal UCB are low (standard deviation, 6.8 fL),[28] or the quantitative phase information provided by qOBM can be applied to estimate average cell volume (following Equation 2).

In addition to incorporating these calculations to estimate the TWBCC, future work will also include autofocusing to ensure that all images provide useful information.

In summary, we have demonstrated the potential of qOBM to quantify WBCs in umbilical cord blood collections bags. Our results show strong agreement with standard hematology analysis. This novel approach is fast, noninvasive, cost efficient, and does not require highly trained personnel to operate, given the automated process. Importantly, it is possible to reproduce the imaging procedure while maintaining a CBU's sterile environment using an integrated bag design that includes the collection bag and optically clear bag. Therefore, qOBM has the potential to reduce costs in CBB, thereby making UCB more accessible for therapy.

CONFLICT OF INTEREST

The authors have disclosed no conflicts of interest.

REFERENCES

1. Mayani H, Wagner JE, Broxmeyer HE. Cord blood research, banking, and transplantation: achievements, challenges, and perspectives. Bone Marrow Transplant 55:48-61 (2020). Available from: http://www.nature.com/articles/s41409-019-0546-9.

2. Dessels C, Alessandrini M, Pepper MS. Factors influencing the umbilical cord blood stem cell industry: an evolving treatment landscape. Stem Cells Transl Med 2018;7:643-50. https://doi.org/10.1002/sctm.17-0244.

3. Panch SR, Szymanski J, Savani BN, et al. Sources of hematopoietic stem and progenitor cells and methods to optimize yields for clinical cell therapy. Biol Blood Marrow Transplant 2017;23:1241-9. https://doi.org/10.1016/j.bbmt.2017.05.003.

4. Gluckman E, Ruggeri A, Volt F, et al. Milestones in umbilical cord blood transplantation. Br J Haematol 2011;154(4):441-7. https://doi.org/10.1111/j.1365-2141.2011.08598.x.

5. Kurtzberg J, Laughlin M, Graham ML, et al. Placental blood as a source of hematopoietic stem cells for transplantation into unrelated recipients. N Engl J Med 1996;335:157-66. https://doi.org/10.1056/NEJM199607183350303.

6. Ballen K, Logan BR, Chitphakdithai P, et al. Excellent outcomes after umbilical cord blood transplantation using a centralized cord blood registry. Stem Cells Transl Med 2018;7:S1–S1. https://doi.org/10.1002/sctm.12353.

7. Ballen KK, Koreth J, Chen Y-B, et al. Selection of optimal alternative graft source: mismatched unrelated donor, umbilical cord blood, or haploidentical transplant. Blood 2012;119:1972-80. Available from: http://www.ncbi.nlm.nih.gov/pubmed/22210876.

8. Spees LP, Martin PL, Kurtzberg J, et al. Reduction in mortality after umbilical cord blood transplantation in children over a 20-year period (1995-2014). Biol Blood Marrow Transplant 2019;25(4):756-63. Available from: https://www.sciencedirect.com/science/article/pii/S1083879118307511?via%3Dihub.

9. Rich IN. Improving quality and potency testing for umbilical cord blood: a new perspective. Stem Cells Transl Med 2015;4: 967-73. https://doi.org/10.5966/sctm.2015-0036.

10. Bart T, Boo M, Balabanova S, et al. Impact of selection of cord blood units from the United States and Swiss registries on the cost of banking operations. Transfus Med Hemother 2013;40: 14-20. Available from: http://www.ncbi.nlm.nih.gov/pubmed/23637645.

11. Murphy A, McKenna D, McCullough J. Cord blood banking and quality issues. Transfusion 2016;56:645-52. https://doi.org/10.1111/trf.13388.

12. Meyer-Monard S, Tichelli A, Troeger C, et al. Initial cord blood unit volume affects mononuclear cell and CD34+ cell-processing efficiency in a non-linear fashion. Cytotherapy 2012;14:215-22. Available from: https://www.sciencedirect.com/science/article/pii/S1465324912706321?via%3Dihub.

13. Allan D, Petraszko T, Elmoazzen H, et al. A review of factors influencing the banking of collected umbilical cord blood units. Stem Cells Int 2013;2013:1-7. https://doi.org/10.1155/2013/463031.

14. Santos SVF, Barros SMO, Santos MS, et al. Predictors of high-quality cord blood units. Transfusion 2016;56:2030-6. https://doi.org/10.1111/trf.13653.

15. Saccardi R, Tucunduva L, Ruggeri A, et al. Impact of cord blood banking technologies on clinical outcome: a Eurocord/Cord Blood Committee (CTIWP), European Society for Blood and Marrow Transplantation and NetCord retrospective analysis. Transfusion 2016;56(8):2021-9. https://doi.org/10.1111/trf.13661.

16. Querol S, Gomez SG, Pagliuca A, et al. Quality rather than quantity: the cord blood bank dilemma. Bone Marrow Transplant 2010;45:970-8. Available from: http://www.nature.com/articles/bmt20107.

17. Laerum OD, Farsund T. Clinical application of flow cytometry: a review. Cytometry 1981;2:1-13. https://doi.org/10.1002/cyto.990020102.

18. Adan A, Alizada G, Kiraz Y, et al. Flow cytometry: basic principles and applications. Crit Rev Biotechnol 2017;37:163-76. https://doi.org/10.3109/07388551.2015.1128876.

19. Coulter WH. High speed automatic blood cell counter and cell size analyzer. Available from: http://whcf.org/wp-content/uploads/2015/05/1956-WHC-NEC-Paper.pdf

20. Saytashev I, Glenn R, Murashova GA, et al. Multiphoton excited hemoglobin fluorescence and third harmonic generation for non-invasive microscopy of stored blood. Biomed Opt Express 2016;7:3449. Available from: http://www.ncbi.nlm.nih.gov/pubmed/27699111.

21. Ledwig P, Robles FE. Epi-mode tomographic quantitative phase imaging in thick scattering samples. Biomed Opt Express 2019;10:3605. Available from: https://www.osapublishing.org/abstract.cfm?URI=boe-10-7-3605.

22. Ledwig P, Sghayyer M, Kurtzberg J, et al. Dual-wavelength oblique back-illumination microscopy for the non-invasive imaging and quantification of blood in collection and storage bags. Biomed Opt Express 2018;9:2743-54. https://doi.org/10.1364/BOE.9.002743.

23. Park Y, Depeursinge C, Popescu G. Quantitative phase imaging in biomedicine. Nat Photonics 2018;12:578-89. Available from: http://www.nature.com/articles/s41566-018-0253-x.

24. Ford TN, Chu KK, Mertz J. Phase-gradient microscopy in thick tissue with oblique back-illumination. Nat Methods 2012;9: 1195-7. Available from: http://www.nature.com/articles/nmeth.2219.

25. Tian L, Waller L. Quantitative differential phase contrast imaging in an LED array microscope. Opt Express 2015;23:11394. Available from: https://www.osapublishing.org/abstract.cfm?URI=oe-23-9-11394.

26. Mohyeddin Bonab MA, Alimoghaddam KA, Goliaei ZA, et al. Which factors can affect cord blood variables? Transfusion 2004; 44:690-3. https://doi.org/10.1111/j.1537-2995.2004.03227.x.

27. Sparrow RL, Cauchi JA, Ramadi LT, et al. Influence of mode of birth and collection on WBC yields of umbilical cord blood units. Transfusion 2002;42:210-5. https://doi.org/10.1046/j.1537-2995.2002.00028.x.

28. Chang Y-H, Yang S-H, Wang T-F, et al. Complete blood count reference values of cord blood in Taiwan and the influence of gender and delivery route on them. Pediatr Neonatol 2011;52: 155-60. Available from: https://www.sciencedirect.com/science/article/pii/S1875957211000386?via%3Dihub.

29. Carpentras D, Laforest T, Künzi M, et al. Effect of backscattering in phase contrast imaging of the retina. Opt Express 2018; 26:6785-95. Available from: https://www.osapublishing.org/abstract.cfm?URI=oe-26-6-6785.

30. Sheppard CJR. Defocused transfer function for a partially coherent microscope and application to phase retrieval. J Opt Soc Am A 2004;21:828. Available from: https://www.osapublishing.org/abstract.cfm?URI=josaa-21-5-828.

31. Sordillo LA, Pratavieira S, Pu Y, et al. Third therapeutic spectral window for deep tissue imaging. International Society for Optics and Photonics; Proc. SPIE 8940, Optical Biopsy XII, 89400V; 2014. https://doi.org/10.1117/12.2040604.

32. Haidekker MA. The Hough transform. In: Advanced Biomedical Image Analysis. Hoboken, NJ, John Wiley & Sons, Inc.; 2010. p. 211-35. https://doi.org/10.1002/9780470872093.ch7.

33. Wold S, Esbensen K, Geladi P. Principal component analysis. Chemom Intel Lab Syst 1987;2(1–3):37-52. Available from: https://www.sciencedirect.com/science/article/pii/0169743987800849.

34. Prahl S. Obtical absorption of hemoglobin 1999. Available from: https://omlc.org/spectra/hemoglobin/index.html.

35. Phelps JE, Vishwanath K, Chang VTC, et al. Rapid ratiometric determination of hemoglobin concentration using UV-VIS diffuse reflectance at isosbestic wavelengths. Opt Express 2010;18:18779. https://doi.org/10.1364/OE.18.018779